



Hydrogen-induced p-d orbital hybridization and tensile strain of PdGa single-atom alloy metallene boosts complete electrooxidation of ethanol

Genlei Zhang^a, Chenyang Hui^a, Zhenzhen Yang^{a,*}, Qi Wang^a, Sheng Cheng^a, Dawei Zhang^{a,*}, Peng Cui^{a,*}, Jianglan Shui^{b,*}

^a School of Chemistry and Chemical Engineering, Anhui Province Key Laboratory of Advanced Catalytic Materials and Reaction Engineering, Anhui Province Key Laboratory of Controllable Chemistry Reaction and Material Chemical Engineering, Hefei University of Technology, Tunxi Road 193, Hefei 230009, PR China

^b School of Materials Science and Engineering, Beihang University, 100191 Beijing, PR China

ARTICLE INFO

Keywords:

Ethanol oxidation reaction
C1 pathway selectivity
Hydrogen-implantation
P-d orbital hybridization
Tensile strain

ABSTRACT

Ethanol oxidation reaction (EOR) at the anode of direct ethanol fuel cells (DEFCs) obeys C1/C2 dual-pathway reaction mechanism, and improving the selectivity of C1 pathway is crucial to the commercialization of DEFCs. Herein, a novel hydrogen-implanted PdGa single-atom alloy metallene (H-Ga₁Pd₁) is designed for optimizing the C1 pathway to achieve greatly enhanced C1 pathway selectivity through electronic and strain engineering. Benefiting from the strong p-d orbital hybridization interaction and tensile strain effect induced by hydrogen-implantation, H-Ga₁Pd₁ exhibits high mass activity of 10.34 A mg_{Pd}⁻¹ and C1 pathway selectivity of 54.7%, both showing an order of magnitude higher than that of commercial Pd/C. Theoretical calculations reveal that the p-d hybridization interaction could effectively accelerate the C-C bond cleavage and tensile strain enable efficient oxidation of CO* and CH₃* produced by the C-C bond cleavage in C1 pathway, enabling H-Ga₁Pd₁ to efficiently catalyze the complete electrooxidation of ethanol through the C1 pathway.

1. Introduction

Direct ethanol fuel cells (DEFCs) directly fueled by liquid ethanol (EtOH) have been recognized as one of the most promising power devices for portable and mobile applications, but their practical application is greatly impeded by the sluggish and incomplete oxidation of EtOH [1–4]. It is generally believed that ethanol oxidation reaction (EOR) follows the C1/C2 dual-pathway reaction mechanism (scheme S1) [5–7]. Obviously, improving the selectivity of C1 pathway is of great significance to improve the energy conversion efficiency of DEFCs. Nevertheless, the existed EOR catalysts generally suffer from low C1 pathway selectivity, even though most of them significantly enhance the catalytic activity and/or long-term stability [8–10]. Therefore, it is critical and urgent to rationally construct active and stable EOR catalysts with high C1 pathway selectivity.

The preferred C1 pathway with maximum energy conversion efficiency is severely hampered because of the high reaction energy barrier of C-C bond cleavage as well as the sluggish oxidation of adsorbed C1 intermediates such as CO* and CH_x* following the C-C bond cleavage [11,12]. Mechanistically, an ideal EOR electrocatalyst should not only

effectively accelerate the C-C bond cleavage, but also have a robust ability to oxidatively remove adsorbed C1 intermediates [13,14]. Up to now, although great progress has been achieved in the development of EOR electrocatalysts, Pt- and Pd-based nanomaterials are still the most favorable candidates in acid and alkaline electrolytes, respectively [15–18]. However, various metrics of their EOR performance, especially the C1 pathway selectivity, urgently need to be improved to meet the demands of the commercialization of DEFCs. To improve catalytic efficiency, one practical and effective approach is to adjust the d-band properties of Pd or Pt to regulate the adsorption/desorption or oxidative dissociation properties of reaction intermediates, through inducing an up- or downshift in the d-band center or constructing orbital hybridization [19–22]. Generally, the upshift of the d-band center facilitates the adsorption of reaction intermediates [23]. However, the strengthened adsorption of poisonous intermediates such as CO* will result in the catalyst poisoning [24]. On the contrary, the downshift of the d-band center will lead to the weakened affinity of the adsorbed intermediates, which effectively alleviates the poisoning and enhances the C1 pathway selectivity, but fails in facilitating the oxidation of carbonaceous intermediates, thus deteriorating the catalytic activity [25]. The

* Corresponding authors.

E-mail addresses: zyang@hfut.edu.cn (Z. Yang), zhangdw@ustc.edu.cn (D. Zhang), cuipeng@hfut.edu.cn (P. Cui), shuijianglan@buaa.edu.cn (J. Shui).

<https://doi.org/10.1016/j.apcatb.2023.123377>

Received 5 September 2023; Received in revised form 29 September 2023; Accepted 7 October 2023

Available online 9 October 2023

0926-3373/© 2023 Published by Elsevier B.V.

contradictive requirements for the position of d-band center mentioned above suggest that it is almost impossible to simultaneously improve the C1 pathway selectivity and other EOR performance metrics such as apparent catalytic activity and CO resistance for Pt- or Pd-based electrocatalysts, only by shifting the position of d-band center. Besides shifting the position of d-band center, orbital hybridization is another highly-concerned method to adjust the d-band properties of Pd or Pt recently, and the effect is remarkable [26,27]. A few recent reports indicate that in C₂₊ alcohol electrooxidation, Pt- or Pd-based electrocatalysts alloyed/doped with p-block atoms featuring p-d orbital hybridization not only facilitate the C-C bond cleavage, but also inhibit the formation of poisonous CO* intermediates, thereby boosting the complete electrooxidation of C₂₊ alcohols [28,29]. Additionally, optimizing the intrinsic reactivity of each active site of electrocatalysts is also one of the most common strategies to improve catalytic efficiency, which can be achieved by controlling the strain effect of catalyst surface [30–33]. For EOR, the tensile strain is beneficial for enhancing the catalytic performance of Pt- or Pd-based catalysts, whereas compressive strain has the opposite effect [34,35]. Inspired by the above discussion, the preparation of tensile-strained Pt- or Pd-based electrocatalysts featuring optimal d-band properties may open up new opportunities for achieving C1 pathway during EOR.

Herein, a new strategy using hydrogen (H) atoms to tailor Pd-based catalysts is addressed by engineering p-d orbital hybridization and tensile strain. According to this, H-implanted PdGa single-atom alloy metallene (H-Ga₁Pdene) featuring strong p-d orbital hybridization and tensile strain is successfully synthesized via a two-step approach, which achieves efficient EOR catalysis in alkaline electrolytes with excellent C1 pathway selectivity. Hydrogen-implantation (H-implantation) not only leads to tensile strain, but also causes the downshift of the d-band center of Pd and strengthens the p-d orbital hybridization interaction between Ga and Pd. With about 15 times improvement of the C1 pathway selectivity relative to that of commercial Pd/C, H-Ga₁Pdene exhibits excellent EOR activity with mass and specific activity of 10.34 A mg_{Pd}⁻¹ and 15.13 mA cm⁻², 10.4 and 6.8 times higher than those of commercial Pd/C, respectively. The catalyst also exhibits superb durability by showing the highest activity retention after chronoamperometry (CA) test and accelerated degradation test (ADT). The further electro-oxidation of CH₃COOK and CO-stripping experiments indicate that C-C bond cleavage and the followed CO* oxidation in C1 pathway can be significantly accelerated by H-implantation. Density functional theory (DFT) calculations reveal that the p-d hybridization interaction can effectively accelerate the C-C bond cleavage in C1 pathway meanwhile suppressing the C2 pathway, while the p-d hybridization interaction as well as the tensile strain effect enable efficient oxidation of C1 intermediates (CO* and CH₃*) produced by the C-C bond cleavage, boosting the C1 pathway selectivity and catalytic performance.

2. Experimental section

Materials, synthesis of Pdene and H-Pdene, calculation of H content, characterization, electrochemical measurements, in situ infrared reflection absorption spectroscopy (IRRAS) and DFT calculations are presented in [Supporting Information \(SI\)](#).

2.1. Synthesis of Ga₁Pdene

10 mg Pd(acac)₂, 4 mg Ga(acac)₃, 4 mg Mo(CO)₆ and 30 mg ascorbic acid (AA) were added into a 10 mL glass vial containing 5 mL oleylamine (OAm) and then ultrasonicated to obtained a yellow transparent solution, and subsequently transferred into a 10 mL Teflon lining. The Teflon lining was transferred into a suitable-size stainless-steel hydrothermal autoclave, sealed and placed in a vacuum drying oven, which was heated at 80 °C for 1 h. After cooling to room temperature, the colloidal product was collected by centrifugation at 12000 rpm for 15 min, and washed several times with a mixture of ethanol and cyclohexane, and

redispersed in 5 mL OAm stored in a vial. The vial was then put in an oil bath and heated to 200 °C for 30 min. After the reaction, the product was collected by centrifugation at 12000 rpm for 15 min, and washed several times with a mixture of ethanol and cyclohexane, dried at 60 °C to obtain the Ga₁Pdene.

2.2. Synthesis of H-Ga₁Pdene

2 mg freshly prepared Ga₁Pdene and 10 mg polyvinyl pyrrolidone (PVP) were dispersed in 15 mL N, N-Dimethylformamide (DMF) by ultrasound in a 30 mL glass bottle. The glass bottle was sealed and placed in an oil bath. After stirring vigorously for 15 min, the mixture was then heated to 160 °C in 20 min and maintained at 160 °C for 8 h under magnetic stirring before it was cooled to room temperature. The resulting product was collected by centrifugation at 12000 rpm for 15 min, washed three times with ethanol, and dried at 60 °C.

2.3. Calculation of C1 pathway selectivity

The yield of possible EOR product can be conducted by high-performance liquid chromatography (HPLC) equipped with a differential detector and a ChromCore Sugar-10 H column (6 μm, 7.8 × 300 mm). Firstly, a long time *i*-t test has been conducted to collect the product to be measure. The concentration of as-produced CH₃COO⁻ and CH₃CHO can be calculated by the standard curve. For the *i*-t test, the catalysts were cast onto a carbon paper electrode to achieve a loading of 0.017 mg_{metal} cm⁻². Each electrolyte was N₂-saturated 1.0 M KOH solution containing 1.0 M EtOH. 50 mL electrolyte was electrolyzed by chronoamperometry with different catalysts to accumulate the total charge (*Q*). Secondly, a series of CH₃COOH and CH₃CHO standard solutions have been made with a stepped concentration. The standard curve can be drawn with the integral area of HPLC peak detected by Shimadzu LC-20A UFLC system, using 5 M H₂SO₄ aqueous solution as the mobile phase, and the concentration of standard solution. Finally, based on the Faraday formula, the Faradic efficiency of as-produced CH₃COO⁻ and CH₃CHO can be calculated as follow:

$$FE = \frac{e \times n \times F}{Q}$$

Where *e* is the number of electrons transferred to CH₃CHO (*e* = 2) or CH₃COOH (*e* = 4), *n* is the total moles of CH₃CHO or CH₃COOH, *F* is the Faraday constant (96485.33289 C mol⁻¹), and *Q* is the total charge.

The FE of the C2 pathway (*FE*_{C2}) is the sum of FEs of acetate and acetaldehyde.

$$FE_{C2} = FE_{CH_3COOH} + FE_{CH_3CHO}$$

and.

$$FE_{C1} (FE_{\text{of the C1 pathway}}) = 1 - FE_{C2}$$

3. Results and discussion

3.1. Characterization of H-Ga₁Pdene

H-Ga₁Pdene is synthesized via a two-step wet chemistry strategy. PdGa single-atom alloy metallene (Ga₁Pdene) is first synthesized and transformed into H-Ga₁Pdene in N, N-dimethylformamide (DMF) in the followed step, resulting in p-d orbital hybridization and tensile strain (see the Experimental Section in SI). The Ga₁Pdene synthesized in the first step is initially characterized by transmission electron microscopy (TEM) and selected-area electron diffraction (SAED), showing that the product with face-centered cubic (fcc) structure owns an ultrathin graphene-like morphology that presents highly curved and flexible nanosheet-like geometry (Fig. S1a and Fig. S2a). The ultrathin character is further confirmed by atomic force microscopy (AFM), and the average thickness is ~0.86 nm (Fig. S2b), representing about four atomic layers

[36]. Although $\text{Mo}(\text{CO})_6$ is employed in this synthesis step, no Mo signal is detected in the final product by X-ray photoelectron spectroscopy (XPS, Fig. S3) [37]. Scanning transmission electron microscopy and corresponding energy dispersive X-ray spectroscopy (STEM-EDS) elemental mapping (Fig. S2c) exhibits the uniform distribution of Ga and Pd elements across the whole metallene. The actual Ga/(Ga+Pd) atomic ratio is determined to be ~ 1.9 at% by inductively coupled plasma optical emission spectroscopy (ICP-OES, inset in Fig. S2c). Moreover, abundant pores can be clearly observed in high-resolution TEM

(HRTEM) images (Figs. S2d and S2e), and the co-existence of crystalline and amorphous structures is confirmed by HRTEM images and corresponding fast Fourier transform (FFT) pattern (Figs. S2f-S2h). As a contrast, Mo-free monometallic Pd metallene (denoted as Pdene) with non-porous surface (Figs. S4a-S4d) is also synthesized using the same strategy without adding $\text{Ga}(\text{acac})_3$. The Pdene with *fcc* structure (Fig. S4e) exhibits identical morphology as Ga_1Pdene with average thickness of about 0.85 nm (Fig. S4f). The tensile strain caused by the graphene-like structure is confirmed by a negative shift in X-ray

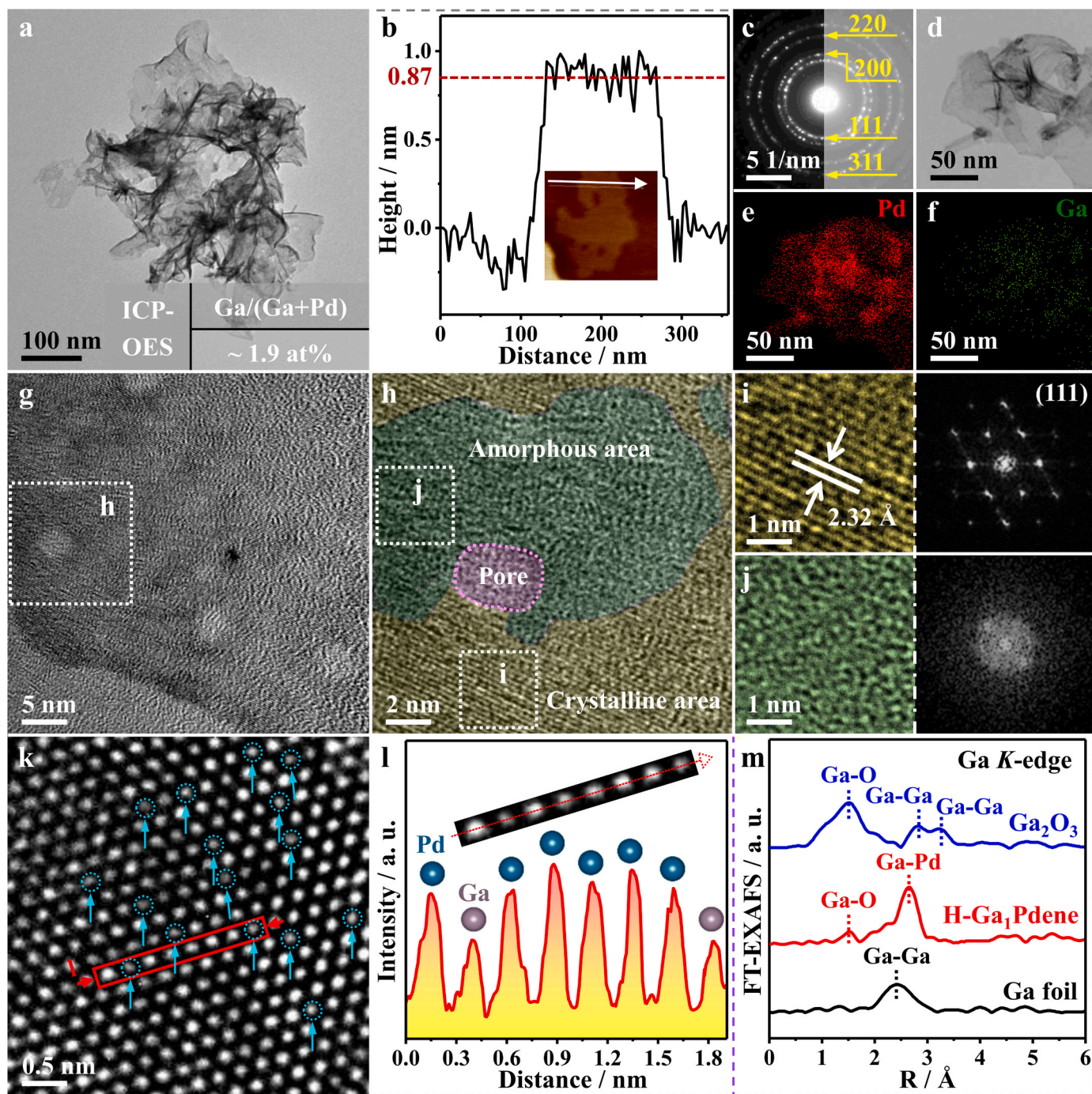


Fig. 1. (a) Low-magnification TEM image, (b) AFM image and corresponding height profile, (c) SAED pattern, (d-f) STEM image and corresponding EDX mapping images, (g) HRTEM image of H- Ga_1Pdene ; (h) Magnified image of the white dashed square region in figure g; (i) Lattice fringes in the crystalline area in Fig. h and the corresponding FFT pattern; (j) Magnified image of the amorphous area in Fig. h and the corresponding FFT pattern; (k) Atomic-resolution AC-HAADF-STEM image of H- Ga_1Pdene ; (l) Atomic intensity line scan profile taken from the red solid rectangle region in figure k; (m) Ga K-edge FT-EXAFS spectra of Ga foil, Ga_2O_3 and H- Ga_1Pdene . The inset of Fig. a shows the actual Ga/(Ga+Pd) atomic ratio of H- Ga_1Pdene measured by ICP-OES; In figure h, pink region represents the pore, yellow and green regions represent crystallization and amorphous areas, respectively.

diffraction (XRD) peaks as compared to the standard Pd (PDF# 46–1043, Fig. S4e), which is consistent with previous reports [38,39]. Lattice parameters calculated based on the (111) peak position are summarized in Table S1, and the lattice constant of Pdene is calculated to be 3.926 Å with about 0.92% tensile strain (relative to the standard Pd, PDF# 46–1043). Besides, compared to the XRD pattern of Ga₁Pdene, the diffraction peaks of Pdene are significantly enhanced, indicating its higher crystallinity (black and blue curves in Fig. S5) [40]. In view of the non-porous surface and higher crystallinity of Pdene, the introduction of Ga may facilitate the formation of pores and amorphous structure. The lattice spacing in the crystalline area of the Ga₁Pdene is about 2.27 Å (Fig. S2g), which is equivalent to that of Pdene (Fig. S4c). Meanwhile, the (111) peak position of Ga₁Pdene is almost the same as that of Pdene (black dotted line in Fig. S5), and the tensile strain of Ga₁Pdene is calculated to be about 0.90% (Table S1). Furthermore, no obvious diffraction peaks related to PdGa alloy are observed in the XRD pattern. To identify the Ga single atoms in Ga₁Pdene, atomic-resolution aberration-corrected high-angle annular dark-field scanning transmission electron microscopy (AC-HAADF-STEM) was performed. Owing to the lower atomic number of Ga (31) relative to Pd (46), the relatively dark dots may be ascribed to the Ga single atoms (marked with pink dashed rings in Fig. S2i). The atomic intensity line scanning profile (Fig. S2j) taken from the orange solid rectangle region marked as j in Fig. S2i exhibits that Ga atoms are dispersed as single atoms in the crystal lattice of Ga₁Pdene. All these results suggest the formation of Ga single atoms in the crystal lattice of Ga₁Pdene.

After H-implantation, many characteristics, such as the metallene morphology, thickness, fcc structure, Ga/(Ga+Pd) atomic ratio, and crystalline/amorphous (C/A) porous surface, are basically unaffected (Fig. 1a–j). Specifically, H-Ga₁Pdene still presents a typical metallene morphology (Fig. 1a and S1b) with an average thickness of ~0.87 nm (Fig. 1b). Besides, H-Ga₁Pdene possesses a typical fcc structure (Fig. 1c), and the crystallinity is significantly enhanced compared with Ga₁Pdene, which is confirmed by XRD (red and blue curves in Fig. S5) and SAED (Fig. S6). STEM-EDS elemental mapping (Figs. 1d–1f) reveals the uniform distribution of Ga on H-Ga₁Pdene, and the Ga/(Ga+Pd) atomic ratio is still ~1.9 at% (inset in Fig. 1a). HRTEM images (Figs. 1g and 1h) and corresponding FFT patterns (Figs. 1i and 1j) identify the porous and C/A interface. The abundant pores are highly desirable for promoting the accessibility of reactants to metallene, to achieve high mass transfer and fast kinetics [41]. Meanwhile, the C/A interface equips the H-Ga₁Pdene with abundant highly-active interfacial atoms [40]. Many structural features of Ga₁Pdene are almost unaffected by H-implantation, however, lattice parameters such as lattice spacing, lattice constant and so on are exceptions. After H-implantation, the lattice spacing of the (111) plane is expanded from 2.27 Å of Ga₁Pdene (Fig. S2g) to 2.32 Å of H-Ga₁Pdene (Fig. 1i). Moreover, H-implantation leads to negative shifts of the XRD peaks (Fig. S5) as well as a smaller radius in the SAED pattern (Fig. S6), further indicating the lattice expansion. Based on the XRD results, the lattice constant and lattice expansion rate of H-Ga₁Pdene are calculated to be 4.014 Å and 3.19%, respectively (Table S1). H-implantation enlarges the Ga₁Pdene lattice, resulting in an increase in tensile strain from 0.90% (for Ga₁Pdene) to 3.19% (for H-Ga₁Pdene), which can be also observed after the hydrogenation of Pdene. After hydrogenation, the lattice spacing of the (111) plane expands from 2.27 Å for Pdene to 2.32 Å for H-Pdene (Figs. S7a–S7c) with XRD diffraction peaks shifting to a lower angle (Fig. S7d). The tensile strain of H-Pdene is calculated to be 3.21% (Table S1), higher than that of Pdene (0.92%). According to Vegard's law [42], the H content in H-Ga₁Pdene (H/(Pd+Ga) atomic ratio) is calculated to be 0.637, which is close to that in H-Pdene (H/Pd = 0.642, Fig. S8 and Table S1). Furthermore, based on the different contrast of Pd and Ga atoms in the atomic-resolution AC-HAADF-STEM image (Fig. 1k), the well-isolated dispersion of Ga single atoms in the crystal lattice of H-Ga₁Pdene can be observed (marked with cyan dashed rings in Fig. 1k). Meanwhile, the atomic intensity line scanning profile acquired from the red solid

rectangle region marked as l in Fig. 1k shows the distribution of isolated low-intensity Ga atoms between the high-intensity Pd atoms in the crystal lattice (Fig. 1l), further proving isolated Ga single atoms in the crystal lattice of H-Ga₁Pdene. To further verify the monodispersed Ga atoms in H-Ga₁Pdene, the extended X-ray absorption fine structure (EXAFS) analysis is carried out. The EXAFS fitting curve of H-Ga₁Pdene is displayed in Fig. S9, and the EXAFS fitting parameters are summarized in Table S2. In the Ga K-edge Fourier transformed EXAFS (FT-EXAFS) spectrum of H-Ga₁Pdene (red curve in Fig. 1m), different from those of Ga foil (black curve in Fig. 1m) and Ga₂O₃ (blue curve in Fig. 1m), the main and minor peaks located at ~2.65 and ~1.52 Å could be assigned to Ga-Pd and Ga-O bonds, respectively, according to the detailed EXAFS fitting parameters (Table S2). No peaks related to Ga-Ga bond (~2.43 Å, ~2.82 Å and ~3.23 Å, Table S2) could be observed, verifying the atomically monodispersed Ga in H-Ga₁Pdene.

The oxidation state and coordination environment of Ga in H-Ga₁Pdene optimized by H-implantation are disclosed by X-ray absorption near-edge structure (XANES) and EXAFS spectra. Ga K-edge XANES spectra (Fig. 2a) exhibit that compared with Ga foil, severe Ga oxidation is noted for Ga₁Pdene as evidenced by the large offset of the orange curve. However, Ga oxidation is significantly attenuated when H is implanted (red curve in Fig. 2a), suggesting the dominant existence of Ga⁰ and the oxidation suppression by H-implantation. This trend is also confirmed by high-resolution Ga 2p XPS spectra of Ga₁Pdene and H-Ga₁Pdene (Fig. 2b), in which Ga^{x+} (0 < x < 3) dominants in Ga₁Pdene while Ga⁰ in H-Ga₁Pdene. Ga atoms in Ga₁Pdene mainly exist in oxidation state with a significant peak at ~1.47 Å assigned to Ga-O bond in the Ga-K edge FT-EXAFS spectrum (Fig. S10 and Table S2). It is of note that the emergence of the distinct peak (~2.60 Å) attributed to Ga-Pd bond and the absence of peaks ascribed to Ga-Ga bond confirm the single-atomic dispersion of Ga, and exclude the Ga₂O₃ formation. However, in contrast, Ga atoms in H-Ga₁Pdene are barely oxidized, which is testified by the almost disappeared Ga-O peak in the Ga-K edge FT-EXAFS spectrum of H-Ga₁Pdene (Fig. 1m). The results of XANES and FT-EXAFS indicate that H-implantation can not only stabilize Ga in metallic state, but also maintain the single-atomic dispersion of Ga. The change of the electronic interaction between Ga and Pd caused by H-implantation is investigated by XPS. The Pd 3d XPS peaks of Pd⁰ in H-Pdene reveal an upshift of ~0.40 eV relative to that in Pdene (Fig. S11), which is primarily due to the implantation of H atoms into Pd lattice and changes to the distribution of electrons [42]. Besides, the relative contribution of Pd²⁺ is greatly reduced in H-Pdene (Fig. S11), which can be attributed to the formation of air-stable Pd hydride in which the Pd atoms are partially ionized by H atoms and thus less easily oxidized on the surface [43,44]. Moreover, Pd 3d XPS peaks of Pd⁰ in Ga₁Pdene are negatively shifted ~0.18 eV in comparison with Pdene (Fig. S12), presenting an obvious electronic interaction between Ga and Pd in Ga₁Pdene. It is obviously seen that after H-implantation, the Ga 2p_{2/3} XPS peak of Ga⁰ in H-Ga₁Pdene is negatively shifted ~0.25 eV (Fig. 2b and Table S3), while the Pd 3d XPS peaks of Pd⁰ shift to a higher binding energy position by ~0.79 eV (Fig. 2c and Table S3), demonstrating that the enhanced electronic interaction between Ga and Pd and thus the redistribution of electrons induced by implanted H atoms. To further assess the enhanced electronic interaction of Ga and Pd in H-Ga₁Pdene upon the H-implantation, the projected density of states (PDOS) is conducted by theoretical modelling. Considering the tensile strain and composition of Pdene, Ga₁Pdene, H-Pdene, and H-Ga₁Pdene, five structural models (Fig. S13 and inset in Fig. 2d), including pristine Pd (111), Pd(111) with 0.9% tensile strain (Pd(111)_{0.9%TS}), Ga₁-doped Pd (111) with 0.9% tensile strain and Ga/(Pd+Ga) atomic ratio of 2.0% (Ga₁Pd(111)_{0.9%TS}), H-implanted Pd(111) with 3.2% tensile strain and H/Pd atomic ratio of 0.64 (H-Pd(111)_{3.2%TS}), H-implanted Ga₁Pd(111) with 3.2% tensile strain and H/(Pd+Ga) atomic ratio of 0.64 (H-Ga₁Pd(111)_{3.2%TS}), are constructed, in which Pd(111)_{0.9%TS}, Ga₁Pd(111)_{0.9%TS}, H-Pd(111)_{3.2%TS} and H-Ga₁Pd(111)_{3.2%TS} stand for Pdene, Ga₁Pdene, H-Pdene, and H-Ga₁Pdene, respectively. The d-band centers of Pd for

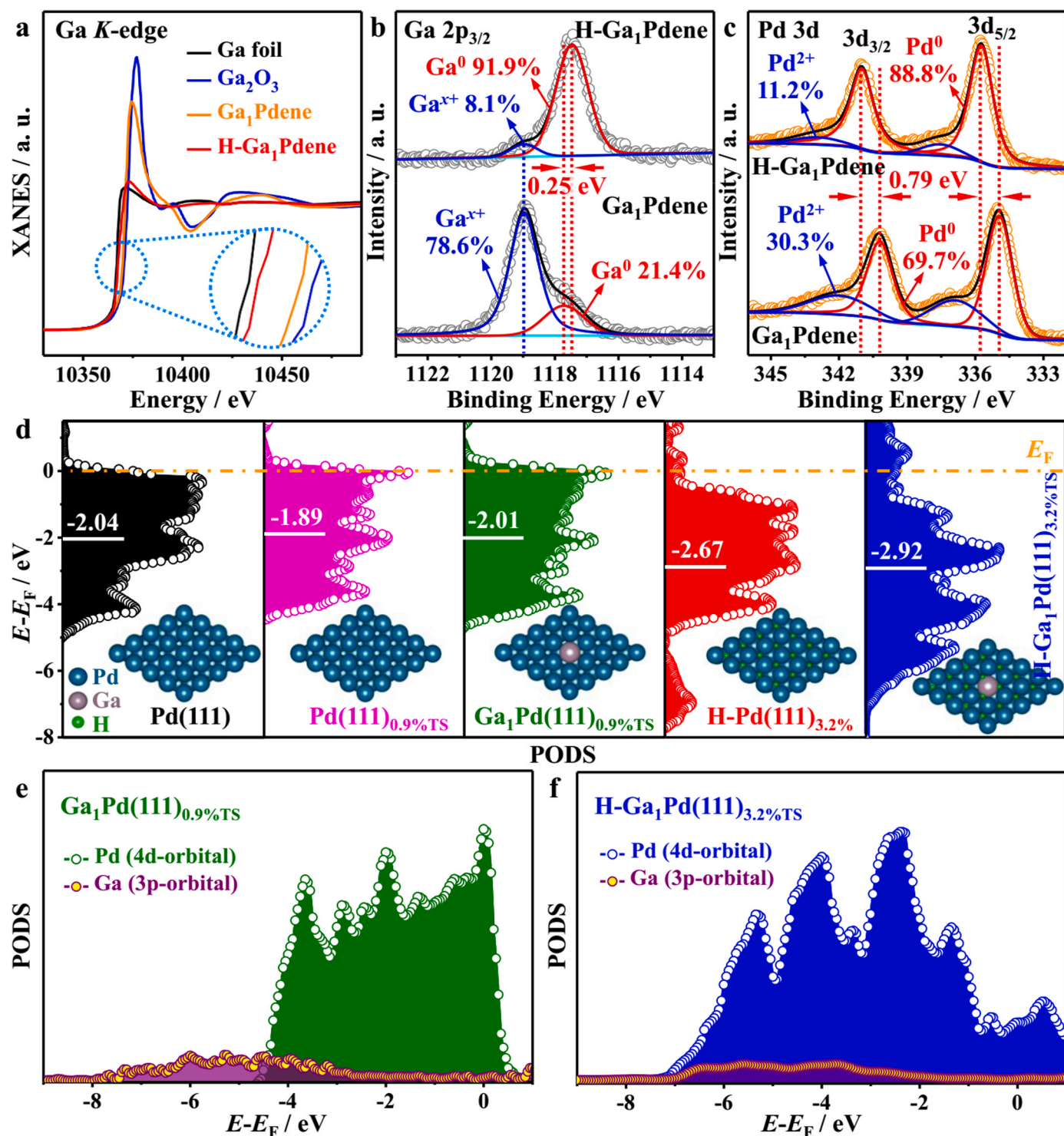


Fig. 2. (a) Ga K-edge XANES spectra of Ga foil, Ga₂O₃ and H-Ga₁Pd; High-resolution (b) Ga 2p and (c) Pd 3d XPS spectra of H-Ga₁Pd and Ga₁Pd; (d) The PDOS of Pd for Pd(111), Pd(111)_{0.9%TS}, Ga₁Pd(111)_{0.9%TS}, H-Pd(111)_{3.2%TS} and H-Ga₁Pd(111)_{3.2%TS} surfaces (the white solid lines and the orange dash line indicate d-band centers of different surfaces and the Fermi level (E_F), respectively); The PDOS of (e) Ga₁Pd(111)_{0.9%TS} and (f) H-Ga₁Pd(111)_{3.2%TS} (inset shows the Pd 4d-orbital and Ga 3p-orbital).

different model surfaces were investigated and clearly displayed in Fig. 2d, in which the d-band centers of Pd(111), Pd(111)_{0.9%TS}, Ga₁Pd(111)_{0.9%TS}, H-Pd(111)_{3.2%TS} and H-Ga₁Pd(111)_{3.2%TS} are -2.04, -1.89, -2.01, -2.67 and -2.92 eV, respectively. Clearly, doping Ga₁ and H-implantation can induce the downshift of the d-band center of Pd, and the lowest d-band center of H-Ga₁Pd(111)_{3.2%TS} originates from the synergistic effect of Ga₁-doping and H-implantation. Theoretically,

alloying or doping p-block atoms into Pd or Pt will generate a p-d orbital hybridization interaction, which has been demonstrated to effectively boost the C-C bond cleavage and oxidation of intermediates in EOR by recent studies [12,28]. Fig. 2e illustrates that the band energy of the Ga 3p-orbital poorly matches with that of the Pd 4d-orbital for Ga₁Pd(111)_{0.9%TS}. However, a perfect matching of band energies of Ga 3p- and Pd 4d-orbital emerges in the plot of the PDOS of H-Ga₁Pd(111)_{3.2%TS}

(Fig. 2f), suggesting H-implantation significantly optimizes the matching of band energy between Ga 3p- and Pd 4d-orbital via downshifting the d-band center of Pd, thereby strengthening the p-d orbital hybridization interaction. The above electronic analysis of Ga₁Pd (111)_{0.9%TS} and H-Ga₁Pd(111)_{3.2%TS} indicates that compared to Ga₁Pdene, there is a stronger electronic interaction between atomic-dispersed Ga and Pd via enhanced p-d orbital hybridization in H-Ga₁Pdene.

3.2. Application of H-Ga₁Pdene for EOR

The EOR was selected to evaluate the electrocatalytic performance based on Ga₁Pdene and H-Ga₁Pdene to investigate the promoting effect of H-implantation. Meanwhile, Pdene and commercial Pd/C (5 wt% of Pd) were chose as reference catalysts. Before evaluation of the electrochemical performance, the as-synthesized H-Ga₁Pdene, Ga₁Pdene and Pdene were uniformly deposited on carbon black (Vulcan XC-72R) to form H-Ga₁Pdene/C, Ga₁Pdene/C and Pdene/C, and the actual Pd loadings measured by ICP-OES are displayed in Table S4. In general, the electrochemical surface area values (ECSAs) of Pd-based catalysts are determined by CO-stripping voltammetry rather than by the underpotentially deposited hydrogen (H_{upd}) region, because the presence of Pd can interfere with the hydrogen desorption and adsorption peak area [45]. Firstly, the ECSAs of the above four catalysts were calculated from the integral areas of the CO oxidation peaks in CO-stripping curves (Fig. S14a), in which H-Ga₁Pdene/C (68.4 m² g_{Pd}⁻¹), Ga₁Pdene/C (63.5 m² g_{Pd}⁻¹), Pdene/C (58.6 m² g_{Pd}⁻¹) exhibit larger ECSAs than commercial Pd/C (45.3 m² g_{Pd}⁻¹) due to the ultrathin 2D structure (Fig. S14b and Table S5). In addition, it can be also seen that the CO oxidation peaks of H-Ga₁Pdene/C, Ga₁Pdene/C, Pdene/C and commercial Pd/C are located at $-0.325 V_{SCE}$, $-0.266 V_{SCE}$, $-0.264 V_{SCE}$ and $-0.252 V_{SCE}$, respectively (Fig. S14a). Obviously, the CO oxidation peak potential of H-Ga₁Pdene/C negatively shifts by 59 mV compared to that of Ga₁Pdene/C, demonstrating that H-implantation endows the H-Ga₁Pdene with substantial improvement in anti-CO poisoning [15, 17]. Moreover, compared to Ga₁Pdene/C, Pdene/C and commercial Pd/C, the reduction peak of Pd for H-Ga₁Pdene/C negatively shifts in cyclic voltammetry curves (CVs) tested in N₂-saturated 1.0 M KOH aqueous solution (Figs. S14c and S14d). This negative shift demonstrates that the binding energy of *OH enhanced and more Pd-OH groups could be formed on H-Ga₁Pdene, which is beneficial to accelerate the oxidation of C1 intermediates and eliminate the poisoning [46]. EOR activity was evaluated in N₂-saturated 1.0 M KOH aqueous solution containing 1.0 M EtOH. The Pd mass and ECSA normalized CVs are displayed in Fig. 3a and S15, and the mass activities (MAs) and specific activities (SAs) for EOR are shown in Fig. 3b and Table S5. It can be clearly seen that the EOR activity of Pdene/C is slightly better than that of commercial Pd/C, and H-Ga₁Pdene/C exhibits a highest peak current density (J_p). Specifically, the MA (4.68 A mg_{Pd}⁻¹) and SA (7.37 mA cm⁻²) delivered by Ga₁Pdene/C are 2.4 and 2.2 times, respectively, higher than those manifested by Pdene/C (1.96 A mg_{Pd}⁻¹/3.34 mA cm⁻²). More impressively, the activity of Ga₁Pdene can be further enhanced after H-implantation, and the MA and SA of H-Ga₁Pdene/C reach up to 10.34 A mg_{Pd}⁻¹ and 15.13 mA cm⁻², respectively, which represent 2.2- and 2.1-fold enhancement compared with Ga₁Pdene/C. The superior MA (SA) delivered by H-Ga₁Pdene/C achieves 10.4 (6.8) times of commercial Pd/C, endowing it as one of the best reported Pd-based alkaline EOR electrocatalysts (Table S6). The onset potential (E_{onset}) in this study is measured by linear scan voltammetry (LSV) and determined as the potential where the current reaches 0.1 mA cm⁻² (Fig. S16) [47]. H-Ga₁Pdene/C produces a more negative E_{onset} ($-0.742 V_{SCE}$, Fig. S16 and Table S7) than Ga₁Pdene/C ($-0.708 V_{SCE}$, Fig. S16 and Table S7), further indicating H-implantation endows H-Ga₁Pdene with substantial enhancement in EOR activity [48]. Moreover, it is worth noting that there exist negative potential shifts of 10% J_p , 50% J_p and J_p ($E_{10\%J_p}$, $E_{50\%J_p}$ and E_{J_p}) from commercial Pd/C, Pdene/C, Ga₁Pdene/C to H-Ga₁Pdene/C (inset in Fig. 3a and Table S7), which indicates an

increasingly lower energy barrier for EOR [28]. All in all, H-Ga₁Pdene/C possess the highest J_p , lowest E_{onset} , $E_{10\%J_p}$, $E_{50\%J_p}$ and E_{J_p} , displaying the outstanding catalytic activity and the lowest energy barrier. In addition to catalytic activity, reaction kinetics is also an important indicator of catalytic performance for catalysts. As depicted in Fig. 3c, H-Ga₁Pdene/C exhibits dramatic growth of activity as the potential increase, illustrating the fastest kinetics for EOR. Meanwhile, the fastest kinetics of H-Ga₁Pdene/C can be further confirmed by the Tafel slope of 90.1 mV dec⁻¹ derived from LSV (Fig. 3d), which is lower to those of Ga₁Pdene/C (190.5 mV dec⁻¹), Pdene/C (218.9 mV dec⁻¹) and commercial Pd/C (255.6 mV dec⁻¹). Noteworthily, if only comparing H-Ga₁Pdene/C and Ga₁Pdene/C, it is obvious that catalytic activity and reaction kinetics for H-Ga₁Pdene/C are comprehensively superior to those for Ga₁Pdene/C, demonstrating that H-implantation can greatly activate Ga₁Pdene.

Besides the exceptional activity and reaction kinetics, the H-Ga₁Pdene/C also exhibits excellent EOR durability. The durability of these catalysts was first evaluated by CA tests performed at $-0.35 V_{SCE}$ in N₂-saturated 1.0 M KOH solution containing 1.0 M EtOH for 7200 s, and the activity retention derived from current-time (*i-t*) curves (Fig. S17a) are depicted in Fig. 3e. Obviously, the activity retention of H-Ga₁Pdene/C is consistently higher than those of the other three catalysts over the entire test range, and after 7200 s, the activity retention of H-Ga₁Pdene/C is 25.2%, much higher than those of Ga₁Pdene/C (18.4%), Pdene/C (11.6%) and commercial Pd/C (7.8%), suggesting its best durability. Generally speaking, durability is specifically reflected in anti-poisoning ability and structural/compositional stability. When CO was bubbled into the N₂-saturated electrolyte during the CA tests, as displayed in Fig. 3f and Fig. S17b, the activities of Ga₁Pdene/C, Pdene/C and commercial Pd/C instantly decreased sharply, especially commercial Pd/C, directly dropped to near zero. However, the activity of H-Ga₁Pdene/C almost kept its initial ongoing tendency. After 7200 s, due to the injection of CO, the active retentions of H-Ga₁Pdene/C, Ga₁Pdene/C, Pdene/C and commercial Pd/C drop to 21.8%, 6.3%, 3.1% and 0.24% with decreases of 13.5%, 65.7% and 73.3% and 96.9% (Fig. 3f), respectively, reflecting the highest anti-CO poisoning ability of H-Ga₁Pdene/C, which has been further confirmed by CO-stripping experiments (Fig. S14a). Meanwhile, the structural/compositional stability of H-Ga₁Pdene/C can be confirmed by ADTs, which was performed by applying potential cycles in N₂-saturated 1.0 M KOH aqueous solution containing 1.0 M EtOH with a scan rate of 50 mV s⁻¹ (Fig. S18). As shown in Fig. 3g and Table S8, the activities of these catalysts declined to different degrees after every 500 potential cycles, and after 2000 consecutive cycles, 83.9% of initial activity for H-Ga₁Pdene/C can be retained, much higher than those for Ga₁Pdene/C (68.3%), Pdene/C (57.8%) and commercial Pd/C (44.7%). After ADTs, although suffering from the highest current density, the nanosheet morphology of H-Ga₁Pdene in H-Ga₁Pdene/C is preserved to a certain extent, but the other three catalysts significantly aggregated (Fig. S19). Meanwhile, both the composition analyzed by ICP-OES and the electronic structure analyzed by XPS show that compared with Ga₁Pdene/C, H-Ga₁Pdene/C retains more initial Ga (Fig. S20) after ADTs as well as the electronic structure of Pd changes less (Fig. S21), demonstrating the structural stability of H-Ga₁Pdene. The above results reveal that H-implantation can greatly stabilize the nanosheet morphology and monodispersed Ga atom, thereby significantly improving the durability. Based on the above analysis, it can be concluded that H-implantation can significantly enhance the anti-CO poisoning ability and structural/compositional stability, endowing H-Ga₁Pdene with superior durability.

3.3. Insights into how H-Ga₁Pdene improved the C1 pathway selectivity

EOR over the highly-active H-Ga₁Pdene in alkaline electrolyte obeys C1 and C2 dual-pathway reaction mechanism, which is confirmed by in situ IRRAS. In the spectra obtained at different potentials (Fig. 4a), two downward bands near 1045 and 1085 cm⁻¹ can be attributed to the C-O

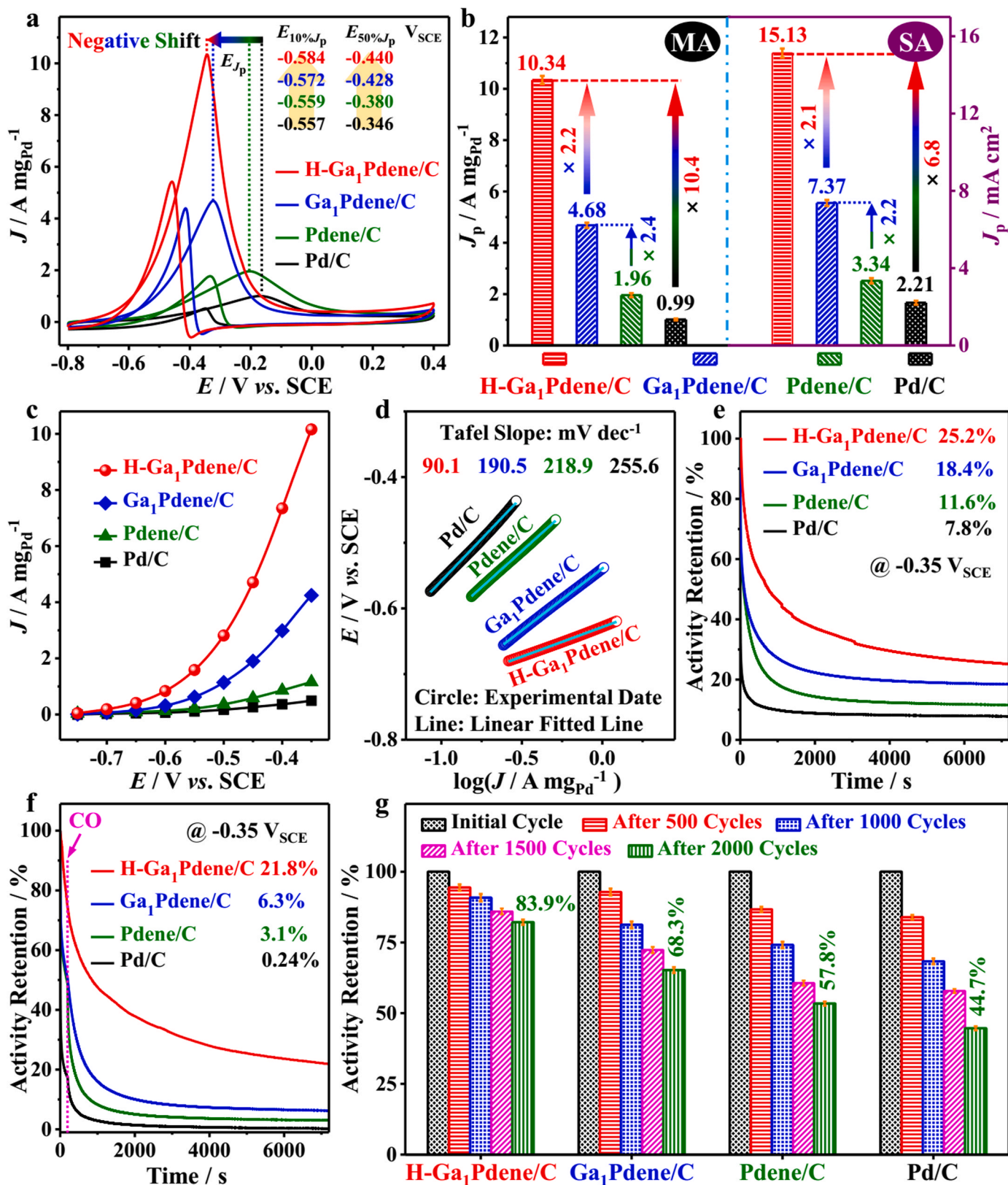


Fig. 3. (a) CVs of H-Ga₁Pdene/C, Ga₁Pdene/C, Pdene/C and commercial Pd/C tested in N₂-saturated 1.0 M KOH aqueous solution containing 1.0 M EtOH with a scan rate of 20 mV s⁻¹; (b) Histogram of MAs and SAs; (c) MA at the indicated potentials; (d) linear regions of the Tafel plots derived from LSVs; (e) Activity retention of the four catalysts within 7200 s derived from CA curves at $-0.35 V_{SCE}$; (f) Response of the four catalysts to bubbling CO during the CA tests performed at $-0.35 V_{SCE}$; (g) Histogram of activity evolutions after every 500 potential cycles of the four catalysts in N₂-saturated 1.0 M KOH aqueous solution containing 1.0 M EtOH with a scan rate of 50 mV s⁻¹.

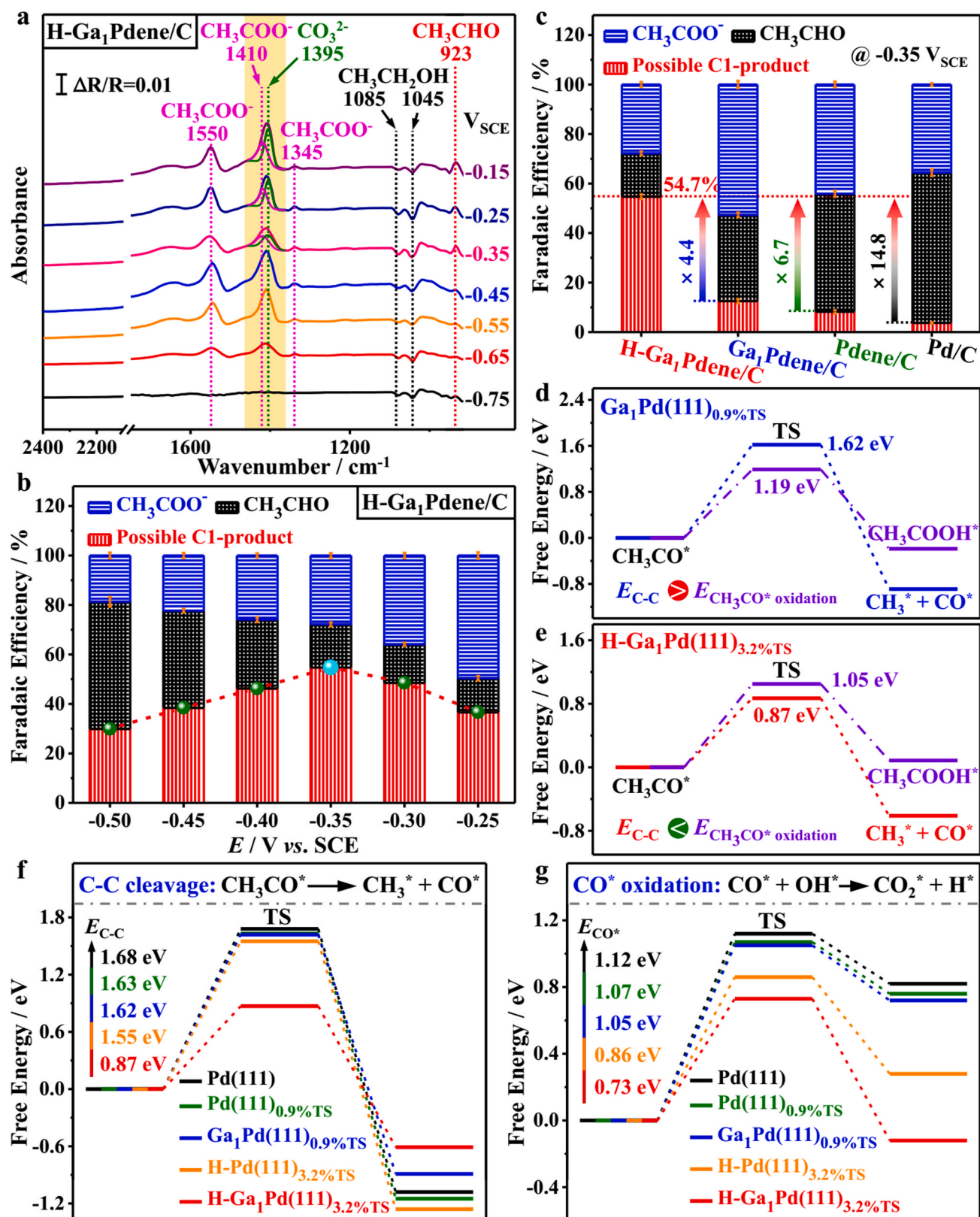


Fig. 4. (a) *In situ* IRRAS spectra for EOR on H-Ga₁Pdene/C at different potentials varying from -0.75 to -0.15 V_{SCE} at an interval of 0.1 V in N₂-saturated 1.0 M KOH aqueous solution containing 1.0 M EtOH; (b) FEs of different products for H-Ga₁Pdene/C at different applied potentials; (c) FEs of different products for H-Ga₁Pdene/C, Ga₁Pdene/C, Pdene/C and commercial Pd/C at -0.35 V_{SCE}; Reaction energy barriers for C-C bond cleavage of CH₃CO* and CH₃CO* oxidation on (d) Ga₁Pd(111)_{0.9%TS} and (e) H-Ga₁Pd(111)_{3.2%TS}; Reaction energy barriers for (f) C-C bond cleavage of CH₃CO* and (g) CO* oxidation on Pd(111), Pd(111)_{0.9%TS}, Ga₁Pd(111)_{0.9%TS}, H-Pd(111)_{3.2%TS} and H-Ga₁Pd(111)_{3.2%TS} (E_{C-C}, E_{CH₃CO*} oxidation and E_{CO*} represent reaction energy barriers for C-C bond cleavage of CH₃CO*, CH₃CO* and CO* oxidation, respectively).

stretching vibration of EtOH [14]. The band near 1400 cm^{-1} (yellow area) can be deconvoluted into a pair of bands located at ~ 1395 and $\sim 1410\text{ cm}^{-1}$, which belong to $\text{HCO}_3^-/\text{CO}_3^{2-}$ (generated CO_2 dissolved in alkaline electrolyte) and acetate (CH_3COO^- , O-C-O symmetric stretching), respectively.¹ Other two downward bands near 1550 and 1345 cm^{-1} can be assigned to CH_3COO^- , corresponding to the asymmetric stretching band of O-C-O and bending vibration of $-\text{CH}_3$ in CH_3COO^- [49]. Moreover, the upward band near 925 cm^{-1} is associated with the C-O stretching vibration of acetaldehyde (CH_3CHO) [50,51]. Therefore, in alkaline electrolyte and using H-Ga₁Pdene/C as the catalyst, EtOH can be oxidized to C2-product (CH_3COO^- and CH_3CHO) and possible C1-product ($\text{CO}_3^{2-}/\text{HCO}_3^-$) via the C2 and C1 pathway, respectively. To explore precise EOR selectivity, the high-performance liquid chromatography (HPLC) quantitative analysis with an external standard curve method (Fig. S22) was adopted to calculate the concentrations of produced CH_3COO^- and CH_3CHO in the reaction residual after a long-term CA test operating at a constant potential [52,53]. The detailed calculation of C1 pathway selectivity for EOR is described in the experimental section in SI. Briefly, the total charge of EOR is first calculated based on the *i-t* curve, and then the amount of charge consumed to generate CH_3COO^- and CH_3CHO is calculated to obtain their Faraday efficiencies (*FE*s), thereby determining the *FE* of possible C1-product (FE_{C1}), i.e. C1 pathway selectivity. Eventually, FE_{C1} of H-Ga₁Pdene/C increases as the applied potential increases from $-0.5\text{ V}_{\text{SCE}}$ to $-0.35\text{ V}_{\text{SCE}}$ but decreases when the applied potential continues to increase, as shown in Fig. 4b and S23. Therefore, $-0.35\text{ V}_{\text{SCE}}$ is selected as the applied potential when evaluating the C1 pathway selectivity for EOR in this study. At $-0.35\text{ V}_{\text{SCE}}$, the FE_{C1} of H-Ga₁Pdene/C is as high as 54.7% (Figs. 4b and 4c), even greater than those of most previously reported Pd-based EOR catalysts (Table S6). By the same method, FE_{C1} s of Ga₁Pdene/C, Pdene/C and commercial Pd/C are calculated as 12.5%, 8.2% and 3.7%, respectively (Fig. S24). Obviously, the FE_{C1} of H-Ga₁Pdene/C is about 4.4, 6.7 and 14.8 times higher than those of Ga₁Pdene/C, Pdene/C and commercial Pd/C (Fig. 4c), respectively, which demonstrates that H-implantation is a powerful strategy to effectively improve the C1 pathway selectivity for EOR.

It is widely accepted that C-C bond cleavage and the followed CO^* oxidation are two rate-determining steps in C1 pathway of EOR [11]. Mechanistically, the as-synthesized high-performance H-Ga₁Pdene should be able to easily break the C-C bond together with effectively promoting the CO^* oxidation, driving the complete electrooxidation of EtOH through the C1 pathway. Specific to the experimental study, the further electrooxidation of $\text{CH}_3\text{COOH}/\text{CH}_3\text{COO}^-$ and CO-stripping experiments can be used to visually evaluate the C-C bond cleavage and CO^* oxidation abilities of catalysts during EOR [54–56]. In this work, electrooxidation of $\text{CH}_3\text{COOH}/\text{CH}_3\text{COO}^-$ was carried out in N_2 -saturated 1.0 M KOH aqueous solution containing 1.0 M CH_3COOK . CVs of the H-Ga₁Pdene/C, Ga₁Pdene/C, Pdene/C and commercial Pd/C tested in N_2 -saturated 1.0 M KOH with and without 1.0 M CH_3COOK are displayed in Fig. S25. It can be clearly seen that there is a noticeable enhanced current density only at H-Ga₁Pdene/C after adding CH_3COOK in KOH solution, while almost no increase for the other three catalysts, indicating that H-Ga₁Pdene/C performs superior in the C-C bond cleavage and hence the electrooxidation of CH_3COOK . Moreover, the results of CO-stripping experiments show that the CO oxidation potential of H-Ga₁Pdene/C is the most negative compared with Ga₁Pdene/C, Pdene/C and commercial Pd/C (Fig. S14a), which fully confirms the superior CO^* oxidation ability of H-Ga₁Pdene. If only focusing on H-Ga₁Pdene and Ga₁Pdene, it is obvious that H-Ga₁Pdene exhibits a significant enhancement in electrooxidation of CH_3COOK as well as CO^* oxidation, suggesting that H-implantation can effectively accelerate C-C bond cleavage and promote CO^* oxidation, thereby improving the C1 pathway selectivity and ultimately the EOR performance.

In order to gain deep insights into the promotion mechanism of H-implantation on C-C bond cleavage and CO^* oxidation in the C1 pathway of Ga₁Pdene-catalyzed EOR, DFT calculations were carried out

on Ga₁Pd(111)_{0.9%}TS and H-Ga₁Pd(111)_{3.2%}TS, standing for Ga₁Pdene and H-Ga₁Pdene, respectively. To better discuss the mechanism, theoretical calculations were also carried out on Pd(111), Pd(111)_{0.9%}TS and H-Pd(111)_{3.2%}TS. It is a remarkable fact that the implantation of H into Ga₁Pdene leads to tensile strain (Fig. 1i) as well as optimizes the p-d orbital hybridization between Ga and Pd (Fig. 2f). Accordingly, we first focus on unraveling the influence of tensile strain and p-d orbital hybridization on C-C bond cleavage. Generally, the combat between the C1 and C2 pathway for EOR in alkaline electrolyte starts from the CH_3CO^* intermediate (as illustrated in Figs. S26a) [53,57]. Therefore, the reaction energy barriers of $\text{CH}_3\text{CO}^* \rightarrow \text{CH}_3^* + \text{CO}^*$ (CH_3CO^* dissociation, i.e. C-C bond cleavage of CH_3CO^*) and $\text{CH}_3\text{CO}^* + \text{OH}^* \rightarrow \text{CH}_3\text{COOH}^*$ (CH_3CO^* oxidation) are important factors determining the selectivity of C1/C2 pathway. If the energy barrier for C-C bond cleavage of CH_3CO^* is lower than that for CH_3CO^* oxidation ($E_{\text{C-C}} < E_{\text{CH}_3\text{CO}^* \text{ oxidation}}$), CH_3CO^* is easier to dissociate via C-C bond cleavage rather than oxidize by OH^* , implying a dominating C1 pathway. Inversely, while $E_{\text{C-C}} > E_{\text{CH}_3\text{CO}^* \text{ oxidation}}$, CH_3CO^* will be inclined to be oxidized by OH^* to form CH_3COOH without C-C bond cleavage, that is, the C2 pathway dominates the EOR [14]. Our calculations show that the $E_{\text{C-C}}$ is higher than $E_{\text{CH}_3\text{CO}^* \text{ oxidation}}$ on Ga₁Pd(111)_{0.9%}TS (Fig. 4d), but lower on H-Ga₁Pd(111)_{3.2%}TS (Fig. 4e), suggesting that CH_3CO^* is inclined to dissociate via C-C bond cleavage on H-Ga₁Pd(111)_{3.2%}TS, further indicating that H-Ga₁Pd(111)_{3.2%}TS largely promotes the C-C bond cleavage of the CH_3CO^* in C1 pathway meanwhile suppressing the C2 pathway. Specifically, as illustrated in Fig. 4f, the $E_{\text{C-C}}$ on Pd(111)_{0.9%}TS (1.63 eV) and H-Pd(111)_{3.2%}TS (1.55 eV) decrease significantly compared with Pd(111) surface (1.68 eV), while Pd(111)_{0.9%}TS (1.63 eV) and Ga₁Pd(111)_{0.9%}TS (1.62 eV) have a similar energy barrier value, which demonstrate that tensile strain can reduce the $E_{\text{C-C}}$ thus favoring the C-C bond cleavage, but monodispersed Ga₁ site can not. Meanwhile, the introduction of tensile strain can also reduce the $E_{\text{CH}_3\text{CO}^* \text{ oxidation}}$ (Fig. S27), which is confirmed by the lower $E_{\text{CH}_3\text{CO}^* \text{ oxidation}}$ on H-Pd(111)_{3.2%}TS (0.97 eV) and Pd(111)_{0.9%}TS (1.07 eV) in comparison with Pd(111) surface (1.12 eV). As expected, the $E_{\text{C-C}}$ to be overcome on Pd(111), Pd(111)_{0.9%}TS and H-Pd(111)_{3.2%}TS are substantially higher than $E_{\text{CH}_3\text{CO}^* \text{ oxidation}}$ (Figs. S26b–S26d), inhibiting the C-C bond cleavage of CH_3CO^* hence blocking the C1 pathway. In addition, Ga₁Pd(111)_{0.9%}TS possesses an increased $E_{\text{CH}_3\text{CO}^* \text{ oxidation}}$ from 1.07 eV to 1.19 eV in comparison with Pd(111)_{0.9%}TS (Fig. S27), but it is still obviously lower than $E_{\text{C-C}}$ (Fig. 4d). However, as for H-Ga₁Pd(111)_{3.2%}TS, compared with H-Pd(111)_{3.2%}TS, $E_{\text{C-C}}$ decreases from 1.55 eV to 0.87 eV (Fig. 4e), even lower than $E_{\text{CH}_3\text{CO}^* \text{ oxidation}}$ (Fig. 4e), indicating that the p-d orbital hybridization interaction between Ga and Pd induced by H-implantation substantially lowers the $E_{\text{C-C}}$ until lower than $E_{\text{CH}_3\text{CO}^* \text{ oxidation}}$, thereby promoting the C-C bond cleavage of CH_3CO^* meanwhile inhibiting CH_3CO^* oxidation. The lower $E_{\text{C-C}}$ in C1 pathway and the higher $E_{\text{CH}_3\text{CO}^* \text{ oxidation}}$ in C2 pathway demonstrate that H-Ga₁Pd(111)_{3.2%}TS exhibits a capability to switch the pathway of EOR from C2 to C1 pathway, mainly originating from the p-d orbital hybridization interaction between Ga and Pd induced by H-implantation. The above evidence together indicates that p-d hybridization interaction between Ga and Pd induced by H-implantation is the most crucial active factor to reduce the $E_{\text{C-C}}$ lower than $E_{\text{CH}_3\text{CO}^* \text{ oxidation}}$, effectively accelerating the C-C bond cleavage of CH_3CO^* in C1 pathway meanwhile suppressing CH_3CO^* oxidation in C2 pathway, thereby realizing the switching of EOR from C2 to C1 pathway.

Subsequently, we calculated the reaction energy barriers of CO^* oxidation (E_{CO^*}) on these five model surfaces to clarify the key factors promoting CO^* oxidation, as displayed in Fig. 4g. The E_{CO^*} are 1.07 and 0.73 eV on Pd(111)_{0.9%}TS and H-Pd(111)_{3.2%}TS, respectively, which are lower than that on Pd(111) surface (1.12 eV), implying tensile strain is beneficial for CO^* oxidation, and the larger the tensile strain, the more favorable the oxidation. Moreover, the E_{CO^*} on H-Ga₁Pd(111)_{3.2%}TS (0.73 eV) is obviously lower than that on H-Pd(111)_{3.2%}TS (0.86 eV), suggesting that p-d hybridization interaction between Ga and

Pd also favors the CO* oxidation. However, the similar values of E_{CO^*} on Pd(111)_{0.9%TS} (1.07 eV) and Ga₁Pd(111)_{0.9%TS} (1.05 eV) indicate that monodispersed Ga₁ site without p-d hybridization interaction between Ga and Pd has almost no enhancement for CO* oxidation. Hence, tensile strain as well as p-d hybridization interaction between Ga and Pd are two vital factors to promote CO* oxidation, together leading to the catalytic activity of H-Ga₁Pd(111)_{3.2%TS} for CO* oxidation tops among the five surfaces, which is confirmed by the lowest E_{CO^*} (Fig. 4g). It is noted that in addition to CO* oxidation, the C1 pathway is also severely limited by the further oxidation of CH₃*, which is one of the other C1 intermediates [29]. Tensile strain and p-d orbital hybridization interaction between Ga and Pd can also reduce the energy barrier of CH₃* oxidation ($E_{\text{CH}_3^*}$, Fig. S28a), where the $E_{\text{CH}_3^*}$ on H-Ga₁Pd(111)_{3.2%TS} is lowest, originating from the tensile strain effect and the p-d orbital hybridization interaction. The lowest $E_{\text{CH}_3^*}$ endows H-Ga₁Pd(111)_{3.2%TS} with the strongest ability to catalyze CH₃* oxidation (Fig. S28a). In addition, the excellent catalytic ability of H-Ga₁Pd(111)_{3.2%TS} for the oxidation of CO* and CH₃* can be further confirmed by the calculated adsorption energy of OH* (E_{OH^*}), which suggest that the strongest E_{OH^*} on H-Ga₁Pd(111)_{3.2%TS} (Fig. S28b). The above results reveal that tensile strain as well as p-d orbital hybridization interaction between Ga and Pd could effectively accelerate the oxidation of CO* and CH₃* formed by the C-C bond cleavage, preventing the poisoning and thus smoothing the C1 pathway for EOR.

To sum up, all EOR performance metrics of H-Ga₁Pdene, including activity (MA and SA), durability, reaction kinetics, E_{onset} as well as C1 pathway selectivity, are comprehensively superior in comparison to other reference catalysts (Fig. S29), originating from the p-d orbital hybridization interaction between Ga and Pd as well as the tensile strain induced by H-implantation. DFT calculations reveal that H-Ga₁Pdene exhibits a pathway switch of ethanol oxidation from C2 to C1 pathway originating from the strong p-d orbital hybridization interaction and the tensile strain effect induced by H-implantation, in which the p-d hybridization interaction effectively accelerates the C-C bond cleavage in C1 pathway meanwhile suppressing the C2 pathway, while the p-d hybridization interaction together with the tensile strain enable efficient oxidation of CO* and CH₃*.

4. Conclusions

In summary, we design and synthesize a new class of H-Ga₁Pdene featuring a strong p-d orbital hybridization interaction and tensile strain effect as an extraordinarily active and stable electrocatalyst for EOR that displays an optimum C1 pathway selectivity of 54.7%, which is 4.4 and 14.8 times higher than those of Ga₁Pdene/C and commercial Pd/C, respectively, topping in the reported Pd-based EOR electrocatalysts. H-implantation not only leads to tensile strain (~3.2%), but also causes a downshift in the d-band center of Pd, which induces a well-matching of band energies between Ga 3p- and Pd 4d-orbital, resulting in an enhanced p-d orbital hybridization interaction between Ga and Pd. Besides the superb C1 pathway selectivity, H-Ga₁Pdene/C also exhibits an excellent activity with MA of 10.34 A mg_{Pd}⁻¹ and SA of 15.13 mA cm⁻², and a long-term durability with 83.9% initial activity retention after ADT of 2000 potential cycles, outperforming those of Ga₁Pdene/C, Pdene/C and commercial Pd/C. Other EOR performance metrics of H-Ga₁Pdene, such as reaction kinetics, E_{onset} and anti-CO poisoning, are significantly optimized and enhanced, and also greatly superior to other three reference catalysts. Moreover, the further electrooxidation of CH₃COOH and CO-stripping experiments indicate that C-C bond cleavage and followed CO* oxidation in C1 pathway can be significantly accelerated by H-implantation. DFT calculations demonstrate that the p-d hybridization interaction can effectively accelerate the C-C bond cleavage in C1 pathway meanwhile suppressing the C2 pathway, while the p-d hybridization interaction as well as the tensile strain effect enable efficient oxidation of C1 intermediates (CO* and CH₃*) in C1 pathway, boosting the C1 pathway selectivity and catalytic

performance. This work provides an effective strategy for the reasonable design of Pd-based electrocatalysts for electrooxidation of multi-carbon organic compounds containing C-C bonds.

CRedit authorship contribution statement

Genlei Zhang: writing-original draft preparation. **Chenyang Hui:** editing and validation. **Zhenzhen Yang:** methodology and research design. **Qi Wang:** investigation. **Sheng Cheng:** curation. **Dawei Zhang:** research design and supervision. **Peng Cui:** funding supporting and supervision. **Jianglan Shui:** supervision.

Declaration of Competing Interest

We declare that we have no known competing financial interests or personal relationships that could have appeared to influence the work reported in this paper.

Data Availability

The authors do not have permission to share data.

Acknowledgments

This work is supported by National Natural Science Foundation of China (21908036), Natural Science Foundation of Anhui Province (2308085MB61).

Appendix A. Supporting information

Supplementary data associated with this article can be found in the online version at doi:10.1016/j.apcatb.2023.123377.

References

- [1] Z. Liang, L. Song, S. Deng, Y. Zhu, E. Stavitski, R.R. Adzic, J. Chen, J. Wang, Direct 12-electron oxidation of ethanol on a ternary Au (core)-PtIr (shell) electrocatalyst, *J. Am. Chem. Soc.* 141 (2019) 9629–9636.
- [2] Y. Zhang, X. Liu, T. Liu, X. Ma, Y. Feng, B. Xu, W. Cai, Y. Li, D. Su, Q. Shao, X. Huang, Rhombohedral Pd-Sb nanoplates with Pd-terminated surface: an efficient bifunctional fuel-cell catalyst, *Adv. Mater.* 34 (2022) 2202333.
- [3] K. Jiang, P. Wang, S. Guo, X. Zhang, X. Shen, G. Lu, D. Su, X. Huang, Ordered PdCu-based nanoparticles as bifunctional oxygen-reduction and ethanol-oxidation electrocatalysts, *Angew. Chem. Int. Ed.* 128 (2016) 9176–9181.
- [4] M. Li, Z. Zhao, W. Zhang, M. Luo, L. Tao, Y. Sun, Z. Xia, Y. Chao, K. Yin, Q. Zhang, L. Gu, W. Yang, Y. Yu, G. Lu, S. Guo, Sub-monolayer YO_x/MoO_x on ultrathin Pt nanowires boosts alcohol oxidation electrocatalysis, *Adv. Mater.* 33 (2021) 2103762.
- [5] G. Zhang, D. Cao, S. Guo, Y. Fang, Q. Wang, S. Cheng, W. Zuo, Z. Yang, P. Cui, Tuning the selective ethanol oxidation on tensile-trained Pt (110) surface by Ir single atoms, *Small* 18 (2022) 2202587.
- [6] Y. Zhu, L. Bu, Q. Shao, X. Huang, Subnanometer PtRh nanowire with alleviated poisoning effect and enhanced C-C bond cleavage for ethanol oxidation electrocatalysis, *ACS Catal.* 9 (2019) 6607–6612.
- [7] B. Lan, Q. Wang, Z. Ma, Y. Wu, X. Jiang, W. Jia, C. Zhou, Y. Yang, Efficient electrochemical ethanol-to-CO₂ conversion at rhodium and bismuth hydroxide interfaces, *Appl. Catal. B-Environ.* 300 (2022), 120728.
- [8] W. Huang, X. Ma, H. Wang, R. Feng, J. Zhou, P. Duchesne, P. Zhang, F. Chen, N. Han, F. Zhao, Promoting effect of Ni(OH)₂ on palladium nanocrystals leads to greatly improved operation durability for electrocatalytic ethanol oxidation in alkaline solution, *Adv. Mater.* 29 (2017) 1703057.
- [9] W. Wang, X. Zhang, Y. Zhang, X. Chen, J. Ye, J. Chen, Z. Lyu, X. Chen, Q. Kuang, S. Xie, Edge enrichment of ultrathin 2D PdPtCu trimetallic nanostructures effectuates top-ranked ethanol electrooxidation, *Nano Lett.* 20 (2020) 5458–5464.
- [10] R. Zhang, Y. Zhao, Z. Guo, X. Liu, L. Zhu, Y. Jiang, Highly selective Pd nanosheet aerogel catalyst with hybrid strain induced by laser irradiation and P doping postprocess, *Small* 19 (2023) 2205587.
- [11] G. Yang, Q. Zhang, H. Yu, F. Peng, Platinum-based ternary catalysts for the electrooxidation of ethanol, *Particuology* 58 (2021) 169–186.
- [12] Y. Wang, M. Zheng, Y. Li, C. Ye, J. Chen, J. Ye, Q. Zhang, J. Li, Z. Zhou, X. Fu, p-d orbital hybridization induced by a monodispersed Ga site on a Pt₃Mn nanocatalyst boosts ethanol electrooxidation, *Angew. Chem. Int. Ed.* 134 (2022) 202115735.

- [13] A. Kowal, M. Li, M. Shao, K. Sasaki, M. Vukmirovic, J. Zhang, N. Marinkovic, P. Liu, A. Frenkel, R. Adzic, Ternary Pt/Rh/SnO₂ electrocatalysts for oxidizing ethanol to CO₂, *Nat. Mater.* 8 (2009) 325–330.
- [14] F. Lv, W. Zhang, M. Sun, F. Lin, T. Wu, P. Zhou, W. Yang, P. Gao, B. Huang, S. Guo, Au clusters on Pd nanosheets selectively switch the pathway of ethanol electrooxidation: amorphous/crystalline interface matters, *Adv. Energy Mater.* 11 (2021) 2100187.
- [15] Y. Fang, S. Guo, D. Cao, G. Zhang, Q. Wang, Y. Chen, P. Cui, S. Cheng, W. Zuo, Five-fold twinned Ir-alloyed Pt nanorods with high C1 pathway selectivity for ethanol electrooxidation, *Nano Res* 15 (2022) 3933–3939.
- [16] Z. Yang, Y. Shi, X. Wang, G. Zhang, P. Cui, Boron as a superior activator for Pt anode catalyst in direct alcohol fuel cell, *J. Power Sources* 431 (2019) 125–134.
- [17] G. Zhang, Y. Shi, Y. Fang, D. Cao, S. Guo, Q. Wang, Y. Chen, P. Cui, S. Cheng, Ordered PdCu-based core-shell concave nanocubes enclosed by high-index facets for ethanol electrooxidation, *ACS Appl. Mater. Interfaces* 13 (2021) 33147–33156.
- [18] Y. Wang, M. Li, Z. Yang, W. Lai, J. Ge, M. Shao, Y. Xiang, X. Chen, H. Huang, A universal synthesis of ultrathin Pd-based nanorings for efficient ethanol electrooxidation, *Mater. Horiz.* 10 (2023) 1416–1424.
- [19] Z. Lyu, X.G. Zhang, Y. Wang, K. Liu, C. Qiu, X. Liao, W. Yang, Z. Xie, S. Xie, Amplified interfacial effect in an atomically dispersed RuO_x-on-Pd 2D inverse nanocatalyst for high-performance oxygen reduction, *Angew. Chem. Int. Ed.* 133 (2021) 16229–16236.
- [20] J. Zheng, G. Li, J. Zhang, N. Cheng, L. Ji, J. Yang, J. Zhang, B. Zhang, Y. Jiang, S. Sun, General strategy for evaluating the d-band center shift and ethanol oxidation reaction pathway towards Pt-based electrocatalysts, *Sci. Chi. Chem.* 66 (2023) 279–288.
- [21] L. Gao, X. Li, Z. Yao, H. Bai, Y. Lu, C. Ma, S. Lu, Z. Peng, J. Yang, A. Pan, Unconventional p-d hybridization interaction in PtGa ultrathin nanowires boosts oxygen reduction electrocatalysis, *J. Am. Chem. Soc.* 141 (2019) 18083–18090.
- [22] Q. Chen, H. Jin, T. Cheng, Z. Wang, Y. Ren, J. Tian, Y. Zhu, Small amounts of main group metal atoms matter: ultrathin Pd-based alloy nanowires enabling high activity and stability towards efficient oxygen reduction reaction and ethanol oxidation, *Nanoscale* 15 (2023) 3772–3779.
- [23] S. Bai, Y. Xu, K. Cao, X. Huang, Selective ethanol oxidation reaction at the Rh-SnO₂ interface, *Adv. Mater.* 33 (2021) 2005767.
- [24] M. Chu, J. Huang, J. Gong, Y. Qu, G. Chen, H. Yang, X. Wang, Q. Zhong, C. Deng, M. Cao, Synergistic combination of Pd nanosheets and porous Bi (OH)₃ boosts activity and durability for ethanol oxidation reaction, *Nano Res* 15 (2022) 3920–3926.
- [25] C. Deng, C.Y. Toe, X. Li, J. Tan, H. Yang, Q. Hu, C. He, Earth-abundant metal-based electrocatalysts promoted anodic reaction in hybrid water electrolysis for efficient hydrogen production: recent progress and perspectives, *Adv. Energy Mater.* 12 (2022) 2201047.
- [26] X. Ai, X. Zou, H. Chen, Y. Su, X. Feng, Q. Li, Y. Liu, Y. Zhang, X. Zou, Transition-metal-boron intermetallics with strong interatomic d-sp orbital hybridization for high-performance electrocatalysis, *Angew. Chem. Int. Ed.* 59 (2020) 3961–3965.
- [27] H. Chen, Q. Wu, Y. Wang, Q. Zhao, X. Ai, Y. Shen, X. Zou, d-sp orbital hybridization: a strategy for activity improvement of transition metal catalysts, *Chem. Commun.* 58 (2022) 7730–7740.
- [28] Y. Qin, W. Zhang, F. Wang, J. Li, J. Ye, X. Sheng, C. Li, X. Liang, P. Liu, X. Wang, Extraordinary p-d hybridization interaction in heterostructural Pd-PdSe nanosheets boosts C-C bond cleavage of ethylene glycol electrooxidation, *Angew. Chem. Int. Ed.* 61 (2022) 202200899.
- [29] L. Ji, H. Che, N. Qian, J. Li, S. Luo, X. Li, X. Wu, Q. Xu, X. Gong, X. Cui, Unconventional spd hybridization in modulating frontier orbitals of carbonaceous radicals on PdBi nanosheets for efficient ethanol electrooxidation, *Appl. Catal. B-Environ.* 328 (2023), 122521.
- [30] Y. Chen, J. Pei, Z. Chen, A. Li, S. Ji, H. Rong, Q. Xu, T. Wang, A. Zhang, H. Tang, Pt atomic layers with tensile strain and rich defects boost ethanol electrooxidation, *Nano Lett.* 22 (2022) 7563–7571.
- [31] M. Luo, S. Guo, Strain-controlled electrocatalysis on multimetallic nanomaterials, *Nat. Rev. Mater.* 2 (2017) 1–13.
- [32] Q. Yao, Z. Yu, L. Li, X. Huang, Strain and surface engineering of multicomponent metallic nanomaterials with unconventional phases, *Chem. Rev.* (2023), <https://doi.org/10.1021/acs.chemrev.3c00252>.
- [33] Z. Xia, S. Guo, Strain engineering of metal-based nanomaterials for energy electrocatalysis, *Chem. Soc. Rev.* 48 (2019) 3265–3278.
- [34] S. Han, Y. Ma, Q. Yun, A.L. Wang, Q. Zhu, H. Zhang, C. He, J. Xia, X. Meng, L. Gao, The synergy of tensile strain and ligand effect in PtBi nanorings for boosting electrocatalytic alcohol oxidation, *Adv. Funct. Mater.* 32 (2022) 2208760.
- [35] H. Mistry, A. Varela, S. Kühn, P. Strasser, B. Cuenya, Nanostructured electrocatalysts with tunable activity and selectivity, *Nat. Rev. Mater.* 1 (2016) 1–14.
- [36] J. Zhang, F. Lv, Z. Li, G. Jiang, M. Tan, M. Yuan, Q. Zhang, Y. Cao, H. Zheng, L. Zhang, Cr-doped Pd metallene endows a practical formaldehyde sensor new limit and high selectivity, *Adv. Mater.* 34 (2022) 2105276.
- [37] K. Zhang, Y. He, R. Guo, W. Wang, Q. Zhan, R. Li, T. He, C. Wu, M. Jin, Interstitial carbon-doped PdMo bimetallic for high-performance oxygen reduction reaction, *ACS Energy Lett.* 7 (2022) 3329–3336.
- [38] M. Luo, Z. Zhao, Y. Zhang, Y. Sun, Y. Xing, F. Lv, Y. Yang, X. Zhang, S. Hwang, Y. Qin, PdMo bimetallic for oxygen reduction catalysis, *Nature* 574 (2019) 81–85.
- [39] M. Xie, S. Tang, B. Zhang, G. Yu, Metallene-related materials for electrocatalysis and energy conversion, *Mater. Horiz.* 10 (2023) 407–431.
- [40] H. Yu, T. Zhou, Z. Wang, Y. Xu, X. Li, L. Wang, H. Wang, Defect-rich porous palladium metallene for enhanced alkaline oxygen reduction electrocatalysis, *Angew. Chem. Int. Ed.* 133 (2021) 12134–12138.
- [41] L. Zhang, Y. Ouyang, S. Wang, D. Wu, M. Jiang, F. Wang, W. Yuan, C. Li, Perforated Pd nanosheets with crystalline/amorphous heterostructures as a highly active robust catalyst toward formic acid oxidation, *Small* 15 (2019) 1904245.
- [42] M. Xie, B. Zhang, Z. Jin, P. Li, G. Yu, Atomically reconstructed palladium metallene by intercalation-induced lattice expansion and amorphization for highly efficient electrocatalysis, *ACS Nano* 16 (2022) 13715–13727.
- [43] J. Fan, J. Wu, X. Cui, L. Gu, Q. Zhang, F. Meng, B.-H. Lei, D.J. Singh, W. Zheng, Hydrogen stabilized RhPdH 2D bimetallic nanosheets for efficient alkaline hydrogen evolution, *J. Am. Chem. Soc.* 142 (2020) 3645–3651.
- [44] Y. Jia, T. Huang, S. Lin, L. Guo, Y. Yu, J. Wang, K. Wang, S. Dai, Stable Pd-Cu hydride catalysts for efficient hydrogen evolution, *Nano Lett.* 22 (2022) 1391–1397.
- [45] Y. Cong, I. McCrum, X. Gao, Y. Lv, S. Miao, Z. Shao, B. Yi, H. Yu, M. Janik, Y. Song, Uniform Pd_{0.33}Ir_{0.67} nanoparticles supported on nitrogen-doped carbon with remarkable activity toward the alkaline hydrogen oxidation reaction, *J. Mater. Chem. A* 7 (2019) 3161–3169.
- [46] D. Wu, K. Kusada, T. Yamamoto, T. Toriyama, S. Matsumura, S. Kawaguchi, Y. Kubota, H. Kitagawa, Platinum-group-metal high-entropy-alloy nanoparticles, *J. Am. Chem. Soc.* 142 (2020) 13833–13838.
- [47] K. Zakaria, M. McKay, R. Thimmappa, M. Hasan, M. Mamlouk, K. Scott, Direct glycerol fuel cells: comparison with direct methanol and ethanol fuel cells, *ChemElectroChem* 6 (2019) 2578–2585.
- [48] L. Luo, C. Fu, F. Yang, X. Li, F. Jiang, Y. Guo, F. Zhu, L. Yang, S. Shen, J. Zhang, Composition-graded Cu-Pd nanospheres with Ir-doped surfaces on N-doped porous graphene for highly efficient ethanol electro-oxidation in alkaline media, *ACS Catal.* 10 (2019) 1171–1184.
- [49] C. Shen, H. Chen, M. Qiu, Y. Shi, W. Yan, Q. Jiang, Y. Jiang, Z. Xie, Introducing oxophilic metal and interstitial hydrogen into the Pd lattice to boost electrochemical performance for alkaline ethanol oxidation, *J. Mater. Chem. A* 10 (2022) 1735–1741.
- [50] A. Geraldes, D. Da Silva, E. Pino, J. Da Silva, R. De Souza, P. Hammer, E. Spinacé, A. Neto, M. Linardi, M. Dos Santos, Ethanol electro-oxidation in an alkaline medium using Pd/C, Au/C and PdAu/C electrocatalysts prepared by electron beam irradiation, *Electrochim. Acta* 111 (2013) 455–465.
- [51] Y. Pan, H. Li, J. Min, J. Xiong, Y. Qin, Z. Wang, Z. Wu, S. Feng, J. Lai, L. Wang, High C1 selectivity in alkaline ethanol oxidation reaction over stable Lewis pairs of Pd-MxC@CNT (M= W, Mo and Cr), *Chem. Eng. J.* 446 (2022), 137178.
- [52] H. Peng, J. Ren, Y. Wang, Y. Xiong, Q. Wang, Q. Li, X. Zhao, L. Zhan, L. Zheng, Y. Tang, One-stone, two birds: alloying effect and surface defects induced by Pt on Cu_{2-x}Se nanowires to boost C-C bond cleavage for electrocatalytic ethanol oxidation, *Nano Energy* 88 (2021), 106307.
- [53] W. Wang, X. Shi, T. He, Z. Zhang, X. Yang, Y. Guo, B. Chong, W. Zhang, M. Jin, Tailoring amorphous PdCu nanostructures for efficient C-C cleavage in ethanol electrooxidation, *Nano Lett.* 22 (2022) 7028–7033.
- [54] S. Song, C. He, J. Liu, Y. Wang, A. Brouzgou, P. Tsiakaras, Two-step sequence for synthesis of efficient PtSn@Rh/C catalyst for oxidizing ethanol and intermediate products, *Appl. Catal. B-Environ.* 119 (2012) 227–233.
- [55] K. Zhang, Y. Shi, S. Li, C. Wang, B. Yan, H. Xu, J. Wang, J. Guo, Y. Du, Au nanochains anchored on 3D polyaniline/reduced graphene oxide nanocomposites as a high-performance catalyst for ethanol electrooxidation, *ChemElectroChem* 4 (2017) 1937–1943.
- [56] G. Wu, R. Swaidan, G. Cui, Electrooxidations of ethanol, acetaldehyde and acetic acid using PtRuSn/C catalysts prepared by modified alcohol-reduction process, *J. Power Sources* 172 (2007) 180–188.
- [57] H. Tian, R. Zhu, P. Deng, J. Li, W. Huang, Q. Chen, Y.Q. Su, C. Jia, Z. Liu, Y. Shen, Ultrathin Pd₃Pt₁Rh_{0.1} nanorings with strong C-C bond breaking ability for the ethanol oxidation reaction, *Small* 18 (2022) 2203506.